https://doi.org/10.5194/tc-2021-45
Preprint. Discussion started: 2 March 2021

The Cryosphere
Discussions

The distribution and evolution of supraglacial lakes on the 79°N Glacier (northeast Greenland) and interannual climatic controls

Jenny V. Turton[1]., Philipp Hochreuther[1]., Nathalie Reimann[1]., Manuel T. Blau[2]
[1]Institute of Geography, Friedrich-Alexander University, 90154 Erlangen, Germany
[2]Pusan National University, Busan, South Korea

Correspondence to: Jenny V. Turton (jenny.turton@fau.de)

Abstract. Together with two neighbouring glaciers, the Nioghalvfjerdsfjorden glacier (also known as 79 North Glacier) drains approximately 12-16% of the Greenland ice sheet. Supraglacial lakes (SGLs), or surface melt ponds, are a persistent summertime feature, and are thought to drain rapidly to the base of the glacier and influence seasonal ice velocity. However, seasonal development and spatial distribution of SGLs in the northeast of Greenland is poorly understood, leaving a substantial error on the estimate of melt water and its impacts on ice velocity. Using results from an automated detection of melt ponds, atmospheric and surface mass balance modelling and reanalysis products, we investigate the role of specific climatic conditions on melt onset, extent and duration from 2014 to 2019. The summers of 2016 and 2019 were characterised by above average air temperatures, particularly in June, as well as a number of rainfall events, which led to extensive melt ponds to elevations over 1400m. Conversely, 2018 was particularly cold, with a large, accumulated snowpack, which limited the development of lakes to altitudes less than 800m. There is evidence of inland expansion and increases in the total area of lakes compared to the early 2000s, as projected by future global warming scenarios.

1 Introduction

Nioghalvsfjerdsfjorden, also known as 79° North Glacier (henceforth 79°N glacier) is a marine terminating glacier on the northeast coast of Greenland. Approximately 8% of the Greenland Ice Stream (GIS) drains into 79°N through the North East Greenland Ice Stream (NEGIS), making it the largest discharger of ice in northern Greenland (Mouignot et al. 2015, Mayer et al. 2018). Prior the 21st century, NEGIS, which extends 600km into the interior of the GIS, was believed to be stable, with little change in ice dynamics (Khan et al 2014, Mayer et al 2018). However, since 2006 NEGIS has undergone pronounced thinning of 1m year^{-1}, and the floating tongue of 79°N has retreated by 2-3km since 2009 (Khan et a 2014). Recently, over 100km^2 of ice was lost through calving of a tributary glacier to 79°N, Spalte Glacier (Figure 1b), following record breaking summer air temperatures in 2019 and 2020, highlighting the vulnerability of this region to climate change and surface melt.

The surface of 79°N and the NEGIS feature persistent melt water ponds, or Supraglacial Lakes (SGL), and meltwater drainage patterns (Figure 1b). SGLs are a frequent summertime feature on many low-elevation glaciers in Greenland (Pope et al 2016), on ice shelves (e.g Larsen C; Luckman et al 2014) and on sea ice (Perovich et al 2002). The albedo of SGLs is between 0.1 and 0.6, depending on their depth (Malinka et al 2018), and therefore absorb much more shortwave radiation than the surrounding solid ice (Buzzard et al 2018a). SGLs influence both the Surface Mass Balance (SMB) and the dynamical stability of glaciers through lowering the albedo at the surface and draining water to the base, which reduces friction and influences ice flow velocity (Zwally et al. 2002; Vijay et al. 2019). Short-lived velocity increases have been observed during summer in a number of marine-terminating glaciers, including 79°N (Rathmann et al 2017). Both Rathmann et al (2017) and Vijay et al (2019) hypothesise that the summer speed-up of

https://doi.org/10.5194/tc-2021-45
Preprint. Discussion started: 2 March 2021

79°N occurs when SGLs drain to the base and alter the subglacial hydrology. SGLs are a key component of the SMB and yet rarely feature in mass balance models or estimates (Smith et al. 2017, Yang et al. 2019). Despite the high number of studies focusing on surface mass loss from the Greenland Ice sheet (e.g Lüthje et al. 2006, Das et al. 2008, Tedesco et al. 2012, Stevens et al. 2015), the relationship between SMB, run-off and SGL development remains unclear.

Despite the widespread occurrence of SGLs, very few studies have investigated the seasonal evolution of SGLs and the atmospheric processes required for their formation in this region. Previous studies have largely focused on Antarctic ice shelves (Langley et al. 2016, Arthur et al. 2020, Leeson et al. 2020) and southern and western Greenland (Lüthje et al. 2006, Das et al. 2008, Tedesco et al. 2012, Stevens et al. 2015). Multispectral satellite products now provide observations of SGL over northeast Greenland at both high-temporal and -spatial resolution, and in many cases free of charge. The northeast of Greenland, and specifically the NEGIS region, has, until recently, lacked such detailed analysis of SGLs, however, this region is likely to show an inland expansion of SGL and ablation zone in the near future (Leeson et al. 2015; Igneczi et al. 2016; Noël et al. 2019). Sundal et al. (2009) used MODIS data to assess the lake area between 2003 and 2007 for 79°N amongst other locations, but likely underestimated the lake area by 12% due to the relatively coarse resolution (250-500m) of the satellite product. Winter estimates of liquid water area are also now available with the newly released Synthetic Aperture Radar (SAR) sensor onboard the Sentinel-1 satellite, which doesn't rely on sunlight, unlike optical sensors (Schröder et al. 2020). Recently, Hochreuther et al. (2021) developed an automated melt detection algorithm for Sentinel-2 satellite data. This provides a near-daily, very-high resolution (10m) time series of SGLs on NEGIS during summertime. In the current study, we use the algorithm developed by Hochreuther et al. (2021) to analyse the interannual SGL spatial evolution and distribution over the 79°N glacier, from 2016 to 2019.

Widespread summer melting was observed over Greenland in 2007, 2010 and 2012 due to the particularly warm summers (Tedesco et al. 2013, Lim et al. 2016, Hanna et al. 2014a, Bonne et al. 2015). In most cases, the northeast of Greenland, especially the coastal regions and marine terminating glaciers, have received little or no attention during these stand-out years, possibly due to weaker teleconnection signals (Lim et al. 2016) or due to low spatial resolution data (Oltmanns et al. 2019). Similarly, prior to the mid 2010's, the majority of melting was located in the southern and western parts of Greenland, leading to vast research for these regions (e.g van de Wal et al. 2005; 2012; Tedstone et al. 2017; Kuipers Munneke et al. 2018). However, after the mid 2010's, the highest melt anomalies were located in northern Greenland, especially in 2014 and 2016 (Tedesco et al. 2016). Recently, a low-permeability ice slab was identified in northeast Greenland and within 79°N Glacier (MacFerrin et al. 2019). The meters-thick, englacial layers of refrozen melt water enhance melting and runoff processes and are sustained with relatively small amounts of melt water from drainage of SGLs (MacFerrin et al. 2019). With a warming climate, it is likely that the ice slabs will become more widespread and persistent, although more research is required to investigate the glacio-hydrology in these regions. In a recent review paper, Flowers (2018) highlighted that further investigation into surface melt water volume, drainage and runoff from marine-terminating glaciers is required.

The specific aims of this study are to investigate: 1) the spatial distribution of SGLs over the 79°N glacier, 2) the life-cycle of lake development, 3) the atmospheric and topographic controls on melt pond evolution in the northeast of Greenland between 2016 and 2019 and 4) whether conditions have changed since the Sundal et al. (2009) study of the region in the early 2000s. To accomplish this, we use a combination of very high-resolution (10m) Sentinel-2 data, high-resolution (1km) atmospheric modelling output from the Polar Weather Research and Forecasting (PWRF) model and surface mass balance estimates from the COSIPY model, as well as in-situ observations.

In Section 2, we introduce the automatic detection algorithm and data used in the study, followed by the results (Section 3). These are separated into topographic (Section 3.2) and climatic (Section 3.3) controls of the SGL formation and spatial distribution. The discussion continues in Section 4 and the research concludes in Section 5.

2 Data and Methods

2.1 Automated SGL detection algorithm

A previously developed SGL detection algorithm applied to Sentinel-2 data between March and September 2016-2019 has been used for melt pond tracking. For a full description of the processes involved in SGL detection, see Hochreuther et al. (2021), however a brief overview is provided here. Sentinel-2 is an earth observation programme run by Copernicus. High-resolution (10-60m) optical imagery is collected from two twin satellites, Sentinel-2 A and B, at a revisit duration of approximately 5 days at the equator. The satellites acquire observations from -56° to 84° latitude over land and coastal areas. Sentinel-2 A satellite was launched in June 2015, whilst Sentinel-2 B was launched in March 2017. Data coverage in 2015 was too low over the study area to extract a meaningful timeseries of SGLs. Therefore, the timeseries used here runs from March 29 2016 to September 19 2019. A total of 39,916 scenes from 12 granules were downloaded from the Google cloud storage repository (https://cloud.google.com/storage/docs/public-datasets/sentinel-2?hl=de, last accessed 24 May 2019). Satellite scenes with less than 90% data coverage were removed from the collection, and only data for days with a full coverage set were considered for further processing. All scenes from the same date were subsequently merged band-wise for the visible bands (2,3 and 4). For more information on pre-processing steps prior to implementing the lake detection algorithm, see Hochreuther et al. (2021).

An empirically developed and locally tuned static band ratio threshold for the blue to red band spectra was applied to delineate ice and slush from liquid water. After sieving the binary mask to reduce noise and retain only water areas larger than 150 pixels (0.015 km2), a topographic shadow mask was applied to the data to avoid misclassifications. Furthermore, as lakes on the Greenland Ice sheet have been shown to form mainly within topographic sinks, only water areas within topographic depressions were retained. Finally, a two-step cloud detection was applied, taking changes of lake area over time (step 1) and cloud (shadow) size into account.

Lakes are not detected on the floating tongue portion of the glacier. Firstly, there are no topographic sinks, as these are reliant on a Digital Elevation Model (DEM) of the grounded ice sheet. Secondly, the tongue is fast moving (approximately 1500m a^{-1}; Krieger et al. 2020), which makes it difficult to track the lake outlines from one year to the next. Finally, melt water on the tongue is extensive and flows in more linear patterns as it drains through crevasses (Figure S1).

2.2 In Situ Observations

Observational data at two AWSs located on Kronprins Christian Land (KPC) in the northeast of Greenland are used from the PROMICE (Programme for Monitoring of the Greenland Ice Sheet) network (https://www.promice.dk, last accessed 3 April 2019), operated by the Greenland and Denmark Geological Survey (GEUS). AWS KPC_U (Upper) is located at 79.83°N, 25.17°W, 870m a.s.l and KPC_L (lower) is located at 79.91°N, 24.08°W, 370m a.s.l (Figure 1). See Table 1 and Turton et al (2019) for more information on data availability and the climatology of this region.

Table 1: Location, elevation and data availability of KPC_L and KPC_U AWSs. Observations are taken approximately 2m about the surface. T is air temperature, SW_{in} and LW_{in} are the incoming (downward) short and longwave radiation respectively. See van As and Fausto (2011) for more information on observations from the PROMICE network.

https://doi.org/10.5194/tc-2021-45
Preprint. Discussion started: 2 March 2021

Name	Location	Elevation (m a.s.l)	Data Availability	Variables used in this study
KPC_L	79.91°N, 24.08°W	380	01.01.2009- present	T, cloud cover SW_{in}, LW_{in}
KPC_U	79.83°N, 25.17°W	870	01.01.2009-14.01.2010, 18.07.2012-present	T, cloud cover SW_{in}, LW_{in}

2.3 Reanalysis data

The European Centre for Medium range Weather Forecasts (ECMWF) 5th generation reanalysis product ERA5 has been developed to replace the ERA-Interim product. ERA5 was gradually released starting in July 2017, and back to 1979 is now available. The horizontal resolution of ERA5 is approximately 31km and has 137 levels in the vertical from the surface to a height of 0.01hPa. Total precipitation and snowfall have been extracted from ERA5 at hourly intervals from the nearest grid point to the coordinates of the AWS. The ratio of snowfall to total precipitation (SF/TP) is then calculated. Total precipitation and snowfall estimates from ERA5 were compared to observations taken from buoy measurements in the Arctic ocean by Wang et al (2019) and found to have a high degree of agreement with observations. The high resolution of ERA5 was also desirable compared to other available reanalysis products in the region.

2.4 Polar Weather Research and Forecasting Model

Archived model output from the Polar Weather Research and Forecast (PWRF) model (v3.9.1.1) is analysed. Meteorological variables are available at daily temporal and 1 km spatial resolution from Turton et al. (2019b) at https://doi.org/10.17605/OSF.IO/53E6Z. PWRF is a polar-optimised version of the WRF model, to better account for sea ice and snowpack processes (Hines et al 2015). The majority of adjustments in Polar WRF compared to regular WRF are located in the Noah land surface module. The model output has been previously evaluated against the in-situ PROMICE weather stations near 79°N Glacier and can successfully represent a number of near-surface meteorological variables for both daily mean and sub-daily timescales (Turton et al. 2020). The full description and justification of the model setup is provided in Turton et al. (2020) and the inner domain location is presented in Figure 1a. Data are available from October 2013 to December 2018.

https://doi.org/10.5194/tc-2021-45
Preprint. Discussion started: 2 March 2021

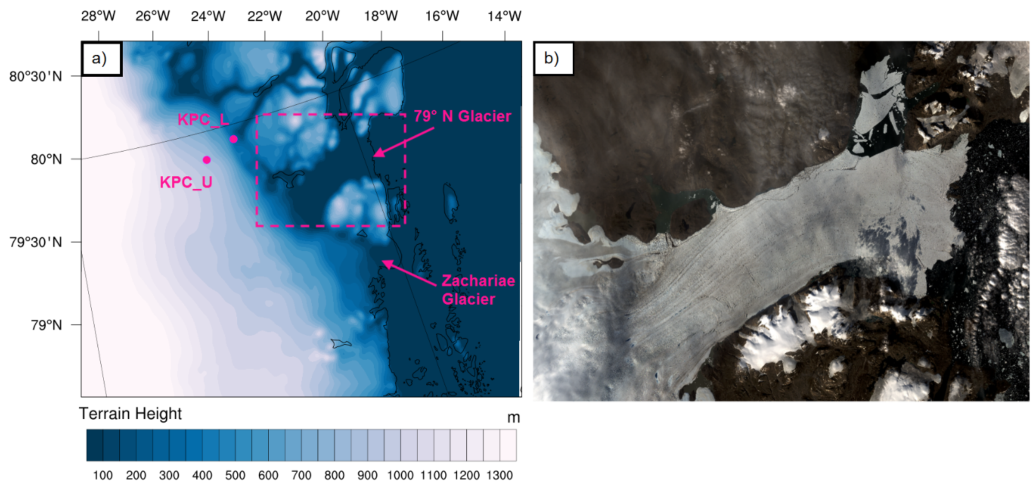

Figure 1: a) The terrain height (colours) of the 79°N Glacier from the Polar Weather Research and Forecasting (PWRF) model simulations by Turton et al. (2020), with the location of the two AWS (KPC_U and KPC_L). The dashed pink box highlights the area shown in b), a Sentinel 2b image taken on August 27th 2020 showing the calving of Spalte Glacier to the north of the main 79°N Glacier floating tongue.

2.5 COSIPY Mass balance model

To provide an overview of the Surface Mass Balance (SMB) of the region, output from a distributed, open-source SMB model called COSIPY (COupled Snowpack and Ice surface energy and mass balance model in PYthon) (https://github.com/cryotools/cosipy; Sauter et al. 2020) is used. Hourly, 1 km spatial resolution Mass Balance (MB) simulations from COSIPY, forced with 4d PWRF output for 2014 to 2018 are used here (COSIPY-WRF). COSIPY-WRF SMB outputs were evaluated against available observations and compared to previous studies by Blau et al. (in review) and found to represent the majority of SMB components with reasonable success at the grounding line and inland for 79°N Glacier. Archived output from COSIPY-WRF is available at: https://doi.org/10.5281/zenodo.4434259. Here, we use surface mass balance estimates from September 2015 to August 2018 to place our melt pond findings into context of the wider melt in the region. For a full list of parameterisations and description of COSIPY, see Blau et al. (in review).

3 Results

3.1 Interannual Characteristics

Previously, Hochreuther et al. (2021) identified SGLs from 2016 to 2019 from Sentinel-2 A and B using a newly developed automatic detection algorithm. Here, we highlight the important lake characteristics and analyse the climatic and topographic controls responsible for the spatial and temporal distribution of SGLs. The average size of individual SGLs varies interannually from a maximum of 0.07 km^2 in 2016 to 0.02 km^2 in 2018.

Lake development typically begins in early June at the lowest elevations. Total lake area increases throughout June and July, reaching a peak in the first week of August. The rate of increase in SGL area varies interannually (Figure 2). The years 2016 and 2019 are characterised by fast increases in SGL area in June (days 150 to 170-180). In 2016, the increasing rate of SGL area regularly exceeded 100% increases in total SGL area from one observation to the next

https://doi.org/10.5194/tc-2021-45
Preprint. Discussion started: 2 March 2021

The Cryosphere
Discussions
Open Access
EGU

(Figure 2). June 2017 had a relatively steady increase in SGL area, with approximately 25% daily increases in area. June 2018 was characterised by a see-saw pattern in expansion of lake area, with periods of fast increases in area (approximately 50% daily increases), followed by two periods of SGL lake closure (Figure 2). Sustained expansion of lake area only occurred after the last week of June. Throughout July, the rate of increase is steady, with approximately 20-25% increase in lake area from one observation to the next in all years (Figure 2). From mid-August (day 220-230), the daily change rate becomes negative as SGLs freeze up or drain. However, there are still individual days of increasing SGL area (positive change rate) punctuating the overall decline in SGL area. SGLs which remain at the end of the melt season (and have not drained into the firn or channels), typically freeze over or become buried in snow. Closure or freeze-over of lakes at the end of the melt season was later and slower in 2018 than in 2016, 2017 and 2019 (Figure 2), and some lakes even remained open at the end of the observation period in mid-September. Freeze over of lakes starts with a growing floe on one side or with a 'lid' in the centre and freezes outwards (Figure 3 arrows). In years with low snow accumulation at the start of September, the frozen, semi-spherical remains of frozen lakes can still be seen.

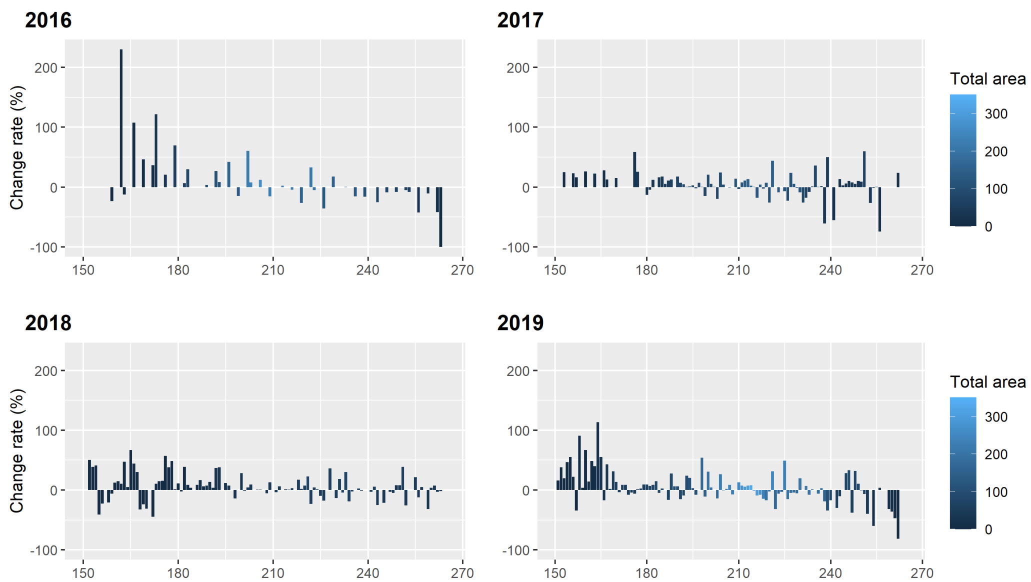

Figure 2: Change rates of the lake area between observations from 2016 to 2019, limited to DOY 150 - 270. Bars coloured by total SGL area (km²).

https://doi.org/10.5194/tc-2021-45
Preprint. Discussion started: 2 March 2021

The Cryosphere
Discussions
Open Access

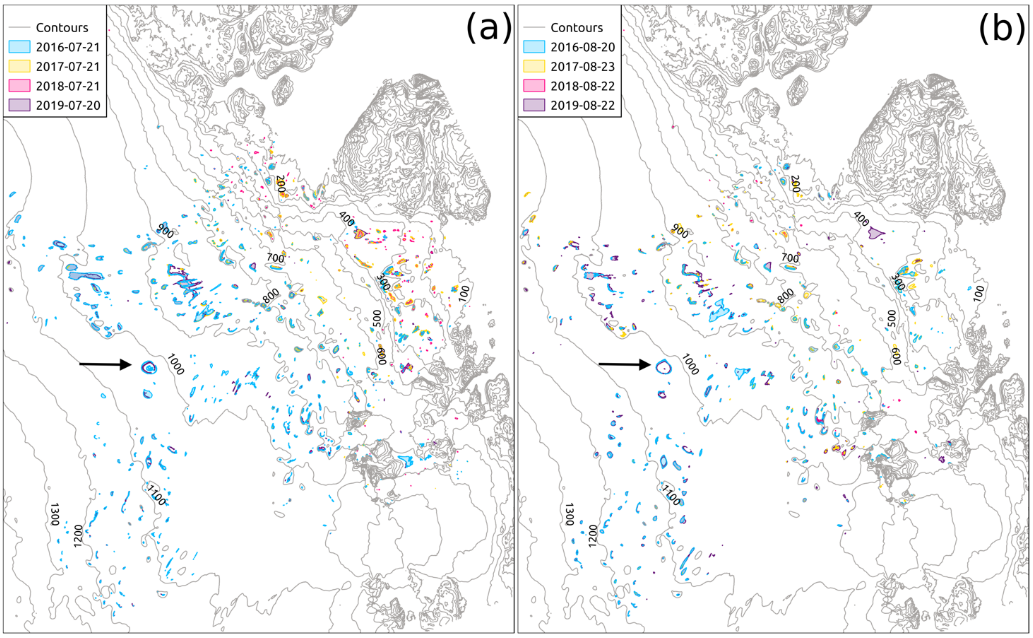

Figure 3: Lake area on July 20/21 (a) and August 20-23 (b) in the four years. Contours are every 100m. Lakes on the tongue have been removed to assess only those controlled by topography. Black arrow points to lake highlighted in the text.

Similar to the rate of change, the total SGL area varies interannually. The largest peak SGL area was seen in 2019, with 330km^2. Conversely, the smallest peak SGL area was in 2018 with just 77km^2 (Hochreuther et al. 2020). This is approximately a 329% increase between maximum lake area in 2018 and in 2019. The difference in the years is shown in Figure 3, where considerably more lakes are highlighted in blue (2016) and purple (2019) than in either 2017 (yellow) or 2018 (pink). Whilst this only shows a snapshot of conditions on two different days, representing peak conditions (mid-July; Figure 3a) and SGL close-up period (mid-August; Figure 3b), the spatial distribution of the lakes differs by years. SGLs at elevations greater than 800m are detected across much of the glacier in 2016 and 2019, but only sparsely in 2017 and 2018. The SGL area in 2016 and 2019 was considerably larger than in 2017 and 2018, especially at altitudes from 1000 to 1300 m a.s.l (Figure 4). However, in years with a lower total SGL area, such as 2018, the distribution of lakes is skewed more towards lower elevations (Figure 4c).

3.2 Topographic Controls

Melt lakes are part of the whole drainage system of ice sheet hydrology. The development of a lake is foremostly controlled by the topography of the ice sheet surface (Lüthje et al 2006). Lakes therefore act as a sink for the englacial channels which distribute the water across and through the ice sheet. The position of lakes on the Greenland Ice Sheet is therefore largely controlled by the underlying bedrock topography (Lampkin and Vanderberg, 2011).

https://doi.org/10.5194/tc-2021-45
Preprint. Discussion started: 2 March 2021

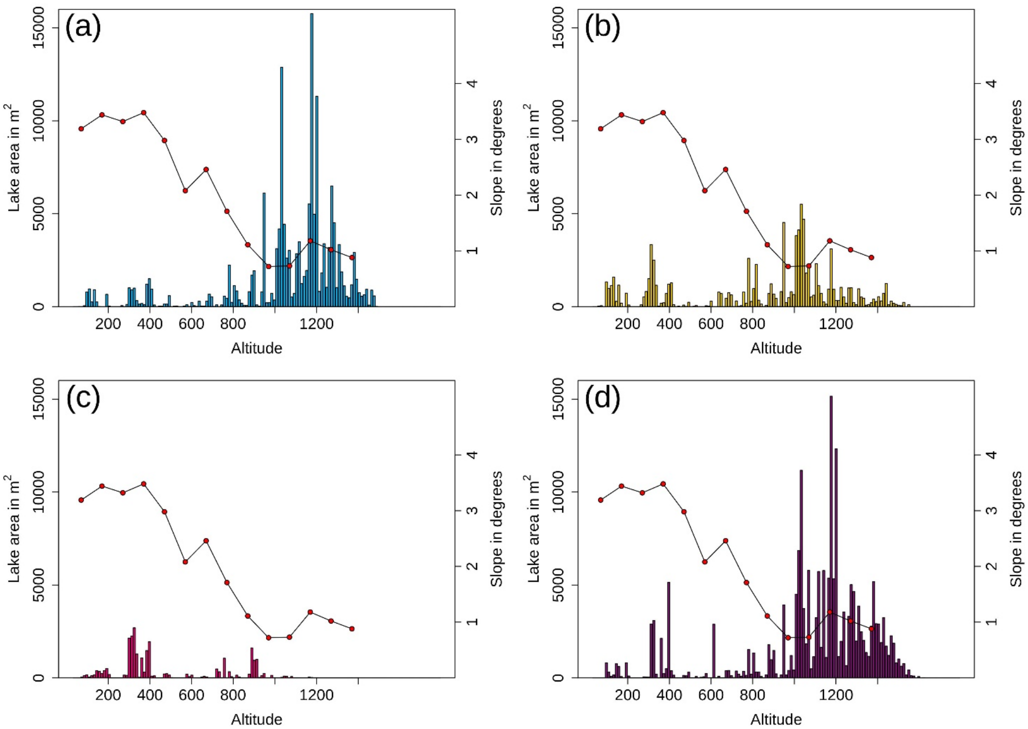

Figure 4: Altitude distribution of lake area for the maxima of 2016 (a), 2017 (b), 2018 (c) and 2019 (d) per 10m altitude difference. Red dots show average slope angle for 100m altitude bins.

Below the grounding line of 79°N Glacier, the lakes move position laterally with the flow of the glacier towards the ocean (not shown). However, above the grounding line, lakes develop in the same position each year (Figure 3). The larger SGL area in 2016 and 2019 compared to 2017 and 2018 is due to the inland (higher elevation) expansion of lake area (Figure 3), as opposed to new areas of the ice sheet developing lakes.

The minimal SGL area between approximately 200 m and 600 m (Figure 4) is partly a consequence of higher slope angle. The slope of the glacier surface between these altitudes is approximately 3 ° to 4 °. The areas with larger SGL area and where the largest lakes develop (Figure 3) is between 0.6° an 1.5° (Figure 4). Unlike some of the ice shelves in Antarctica, where SGLs are concentrated around the grounding line due to low elevation and slope (Arthur et al. 2020), on 79°N Glacier, SGLs are also clustered at higher altitudes, where low slope angles are also measured. Consequently, the largest lakes can be found at altitudes between 850m and 1000m. The highest elevation of SGL development was at 1600m in 2019 (Figure 4). Due to the flat terrain, these lakes are, judging from the blue spectrum saturation, comparatively shallow, whereas the lakes close to the grounding line appear smaller in area but deeper (not shown).

In many cases, the SGLs re-appear each year in the same depression or location as in previous years. Whilst the location of the individual lake is controlled by topographic features, whether or not the lake will develop is due to atmospheric conditions.

3.3 Climatic Controls

https://doi.org/10.5194/tc-2021-45
Preprint. Discussion started: 2 March 2021

In conjunction with the topographic controls, the second most important control for lake development is the availability of melt water, which is largely controlled by the weather conditions. We have assessed numerous atmospheric variables for the four-year period, in an attempt to investigate the relationship between these variables and the melt onset and extent.

Buzzard et al (2018a) investigated the impact of varying atmospheric variables in an idealised 1-D melt pond model and identified that near-surface air temperature (Ta), skin temperature (Tsk), shortwave incoming radiation (SWin) and snowfall (SF) had a considerable impact on the development of SGLs. We investigate these variables in conjunction with rainfall following the findings of Oltmanns et al (2019). Other previously investigated variables which had little to no influence on SGL development include wind speed and non-climatic variables such as wet-snow albedo (Buzzard et al. 2018a), which we do not investigate.

3.3.1 2016 Climate Conditions

The average summer (JJA) Ta is 0.7°C over the floating tongue of the glacier, decreasing to -1.2 °C at an elevation of 830 m a.s.l observed at KPC_U AWS (Turton et al 2019). The average June, July and August air temperatures at KPC_L (KPC_U) are 1.1 °C (-2.1 °C), 3.6 °C (0.7 °C) and 0.5 °C (-2.6 °C) respectively (see Figure 1 for AWS locations). Typically (from 2009-2019), the daily average Ta reaches 0 °C in the second week of June at approximately 390 m a.s.l (KPC_L location), and late June at 830 m a.s.l (at KPC_U location) (Table 2). From this date until mid-August, the daily air temperatures are often at or just above the melting point (Figure 5).

In 2016, all three summer months observed above average Ta at both observation sites. In 2016, at higher elevations, daily Ta reached 0°C slightly earlier than usual (June 11), after a cooler than average start to June, especially at KPC_U (Figure 5b). Rather than a gradual increase in air temperatures throughout the start of June, there was a marked jump in temperature between June 5 and June 11 (Figure 5a,b). At KPC_U the temperature increased from -10.1°C on June 5 to 0.9°C on June 11, and then remained above or close to freezing (0°C +/- 0.75°C) until mid-August (Figure 5b). Just 16 days after this temperature jump, SGL formed at elevations of approximately 870 m a.s.l (elevation of KPC_U) (Table 2). There were 84 days (70 of which were consecutive) with daily Ta higher than 0°C in 2016 at KPC_L (Table 2). The longest consecutive period with above average air temperatures at both KPC_L and KPC_U, from observations between 2009 and 2019, was during 2016.

The average June air temperature, simulated by PWRF, was above freezing for large parts of the NEGIS region (Figure 6a). Spatially, these higher air temperatures approximately follow the 800m contour line, showing some agreement to the altitude-temperature relationship. However, the July average air temperatures deviate from this relationship, with warmer air temperatures above 1200m for the 79°N Glacier but remaining below 800m near Zachariae and to the south of the glacier (Figure 7a). Average July Ta above 3°C is simulated for large parts of NEGIS. At KPC_L, July 2016 was 3.2°C warmer than average, agreeing well with the PWRF data.

In terms of the skin temperature (TSK) of the glacier at KPC_L location, 2016 stands out. When daily average TSK is at 0°C, the term TSK_{melt} is used in this manuscript. The largest number of TSK_{melt} days and longest number of consecutive TSK_{melt} days were observed in 2016 (64 days, of which 47 were consecutive). Similarly, the earliest onset of TSK_{melt} was observed in 2016: June 9th (the average melt day onset is June 18th at KPC_L). At KPC_U, the number of TSK_{melt} days and consecutive TSK_{melt} days are also above average for 2016.

https://doi.org/10.5194/tc-2021-45
Preprint. Discussion started: 2 March 2021

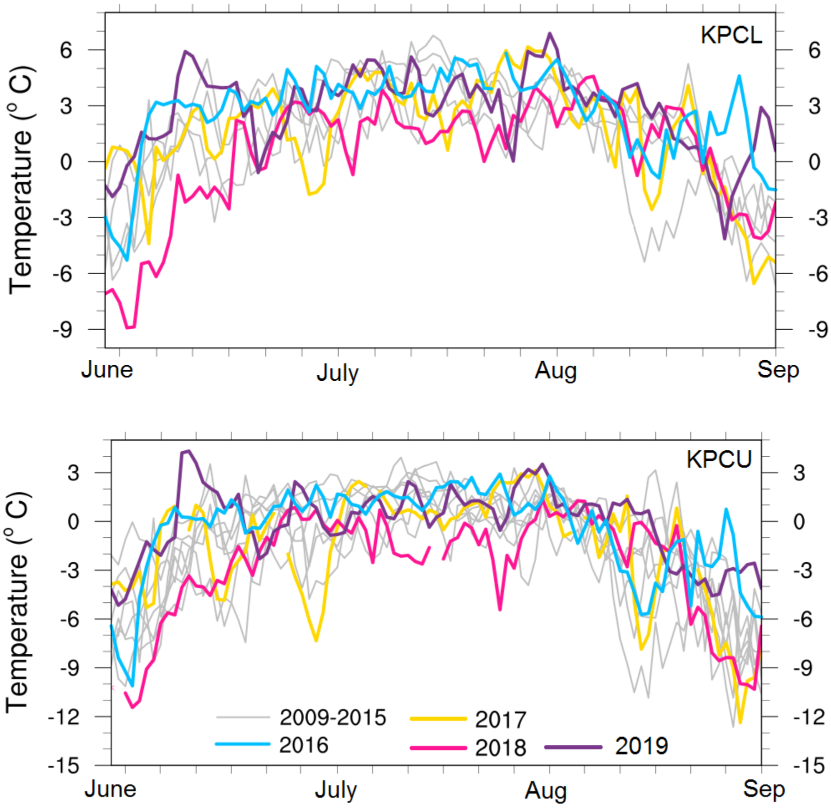

Figure 5: The daily air temperature observations from KPC_L (top) and KPC_U (bottom) from June to September. Grey lines represent data from 2009-2015 (when available). 2016 (blue line), 2017 (yellow line), 2018 (pink line) and 2019 (purple line) are overlain.

Shortwave incoming radiation (SWin) was identified as an important variable for effecting the growth of melt ponds by Buzzard et al (2018a). In 2016, June and July both experienced positive biases in SWin at both observation sites. At KPC_L, the SWin was 7.3Wm^{-2} and 16.7Wm^{-2} higher than average for June and July (respectively). At KPC_U, a positive bias of 10.2Wm^{-2} during June and 6.4Wm^{-2} in July was observed in 2016. There was also a positive bias of 17.3Wm^{-2} and 7.5Wm^{-2} observed in July 2017 (KPC_L and KPC_U respectively). This increase in SWin observed at the surface is attributed to less cloud cover in the region. Cloud cover (fraction) at the KPC stations is estimated from downwelling longwave radiation and air temperature (both of which are observed) (Van as 2011). There was a reduction in cloud cover fraction in June, July and August in 2016 at both locations. The average summer cloud cover fraction at both locations is 0.4, whereas in 2016 it was 0.3. The reduced cloud cover is further evident in the sentinel images, with many more clear-sky days over NEGIS in 2016 than 2017 or 2018.

As precipitation is not observed at the KPC stations, we have used ERA5 data. Following Wang et al (2019), a high ratio of snowfall to total precipitation can be inferred as more snow, whereas a low ratio means more precipitation fell as rain than snow. Between September 2015 and May 2016 (accumulation period), 160mm of cumulative snowfall fell at the KPC_U location. The ratio of snowfall to total precipitation was 1.0, meaning that all precipitation fell as snow. However, during summer, especially July and August, some rainfall is present in the region (Figure 8). In July

https://doi.org/10.5194/tc-2021-45
Preprint. Discussion started: 2 March 2021

The Cryosphere Discussions
Open Access
EGU

2016, all 7.7mm of cumulated precipitation was liquid rain (ratio of 0), and in August, the ratio was 0.82 with 1.9mm of rainfall. For the whole summer period (JJA), the ratio was 0.5. Even though the summer was therefore relatively dry, there was still a larger amount of summer rainfall in 2016 than in other years.

Summer 2016 experienced the largest average individual SGL size (0.07 km^2), second largest total SGL area and second fastest rate of SGL area growth in our four-year record. A combination of above average air temperatures, particularly in mid-June and July, and a large amount of liquid precipitation during summer was likely responsible for the rapid SGL development and peak in total SGL area in late July.

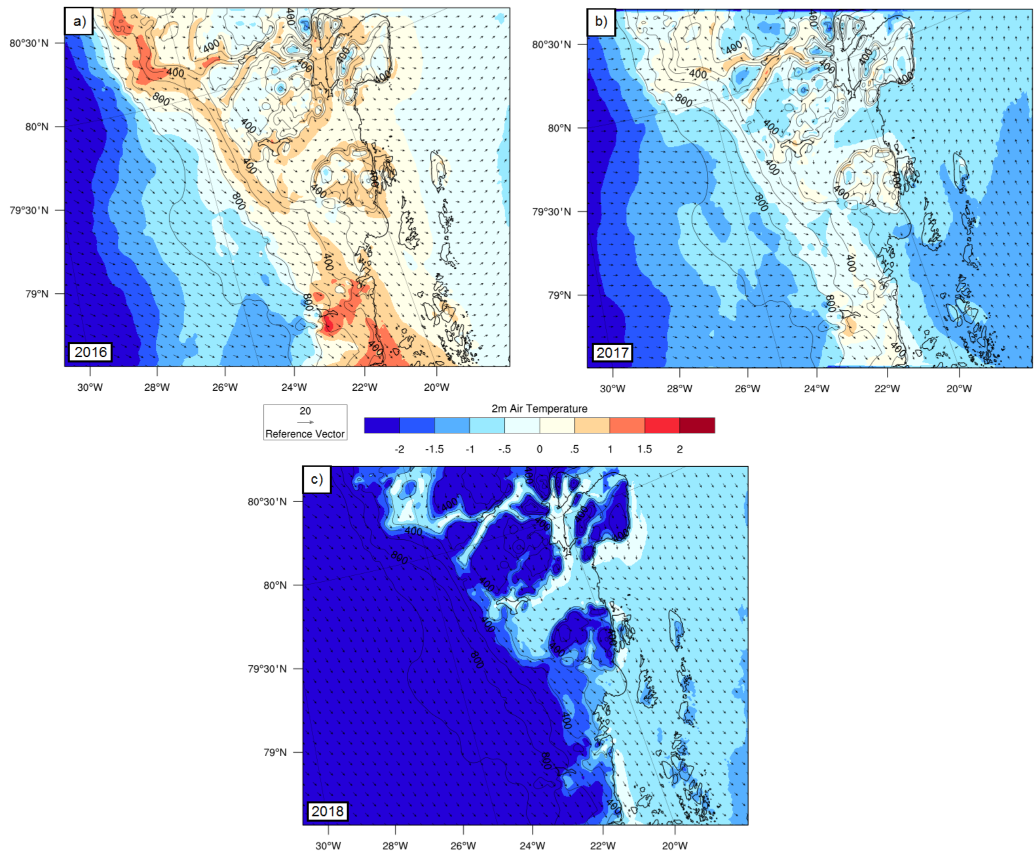

Figure 6: The monthly average 2m air temperature from PWRF runs for June 2016 (a), 2017 (b) and 2018 (c). Simulations were not available for 2019. Contours are every 200 m, with labels every 400 m.

3.3.2 2017 Climate Conditions

The earliest observation of daily Ta above the melting point (from 2009 to 2019) was May 27 2017 at KPC_L. However, air temperatures rapidly decreased again at the end of May, before reaching 0°C on June 1st (Figure 5). Both June and August average air temperatures at both observation sites were slightly below average, but the July average temperature was 0.5°C (0.2°C) warmer than the 2009-2019 average at KPC_L (KPC_U). Despite the lower June Ta compared to 2016, the length of time between Ta reaching above 0 °C at KPC_L and development of melt ponds at 370 m a.s.l. was also 14 days. However, at higher altitudes, there were only 5 days between Ta above 0°C and melt ponds developing at 870 m a.s.l. (Table 2).

https://doi.org/10.5194/tc-2021-45
Preprint. Discussion started: 2 March 2021

The Cryosphere Discussions
Open Access
EGU

The cooler air temperature relative to the previous summer is evident over the majority of NEGIS, with above air temperature locations restricted to low elevation pockets (Figure 6b). The average air temperature is spatially more similar to the 2016 situation in July (Figure 7). In July, Ta greater than 0°C was simulated over much of the 79°N Glacier, up to elevations greater than 1000 m a.s.l. Lower elevation regions, and areas of seasonally exposed rocks reached daily average Ta of 3°C (Figure 7b).

The SWin was lower than average at both observation sites in June 2017 (-2.6 Wm^{-2} at KPC_U and -10.5 Wm^{-2} at KPC_L). There was a positive bias in SWin of 17.3 Wm^{-2} and 7.5 Wm^{-2} observed in July 2017 (KPC_L and KPC_U respectively), revealing clear skies in July. At lower elevations, this positive bias continued into August, with a monthly average bias of 6.7 Wm^{-2} at KPC_L. However, at KPC_U, a negative bias of -8.5 Wm^{-2} was observed.

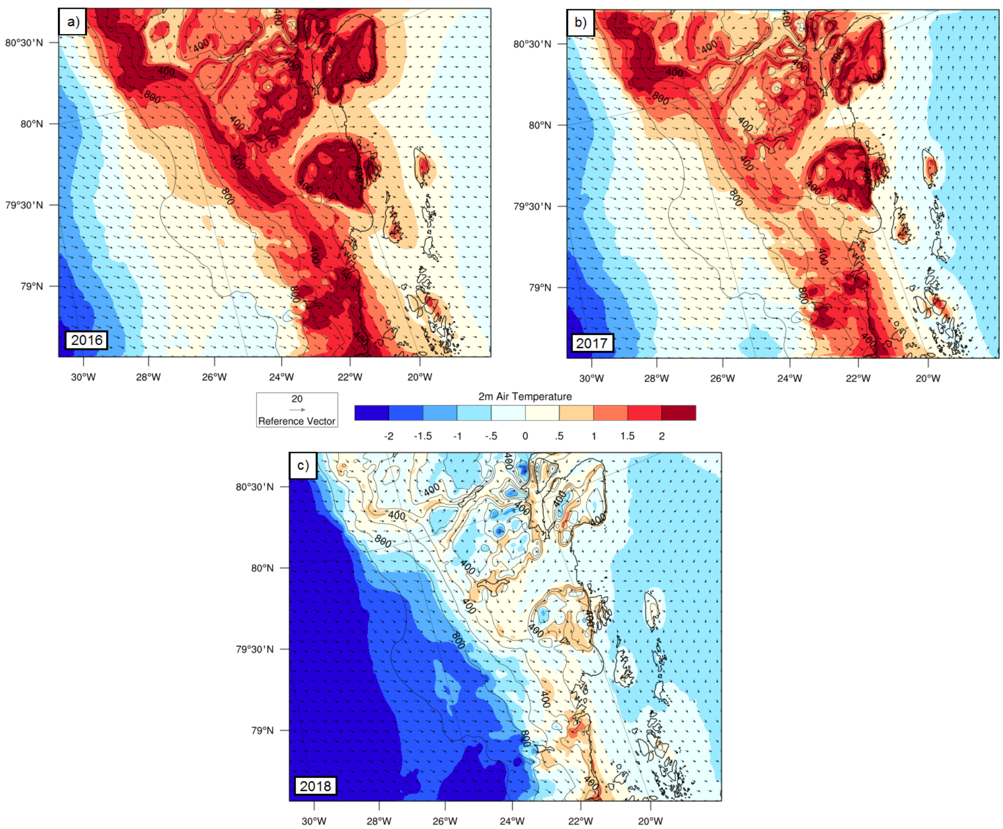

Figure 7: The monthly average 2m air temperature from PWRF runs for July 2016 (a), 2017 (b) and 2018 (c). Simulations were not available for 2019. Contours are every 200 m, with labels every 400 m.

Total accumulated snowfall between September 2016 and May 2017 at KPC_U was approximately 130 mm w.e, which is the second lowest total amount in our four-year period of interest (Figure 8). The summer (JJA) snowfall to total precipitation ratio was 0.96, highlighting the minimal rainfall in this year; the smallest rainfall total in the four-year period. Despite the early observation of Ta above freezing, the earliest in our four-year period, the June average Ta was slightly below average. This, combined with the slightly above average July temperatures, likely led to the slower rate of increase in SGL area compared to 2016 (Figure 2), and peak in maximum area in early August. The thinner

https://doi.org/10.5194/tc-2021-45
Preprint. Discussion started: 2 March 2021

The Cryosphere Discussions
Open Access
EGU

snowpack and limited amount of liquid precipitation falling during summer contributed to the lower maximum SGL area of 153.26 km^2, compared to 265.39 km^2 in 2016.

At higher elevations, the earliest closure of SGLs was observed in this year (September 1st at 870 m a.s.l), which was approximately 10 days after the Ta dropped below freezing at KCP_U. Similarly, at lower elevations, 2017 saw the earliest melt pond closure on September 12th, 18 days after Ta dropped below freezing at KPC_L (Table 2).

Table 2: The timing of the first (last) daily average Ta greater than 0°C (Ta>0°C), number of days with daily Ta greater than 0°C and earliest development (freeze up) of melt ponds at elevations closest to the AWS elevations. 370m a.s.l. relates to KPC_L elevation and 870m a.s.l. relates to KPC_U elevation. *One day observed just below 0°C in this period. ** end of sensing period

Year	AWS	Ta>0°C	# days Ta>0°C (consecutive)	Melt ponds develop at 370m/870m elevation	Ta consistently <0°C	Melt ponds freeze over at 370m/870m
2016	KPC_L	June 7	84 (70*)	June 21	Aug 30	Sep 18**
	KPC_U	June 11	79 (44)	June 27	Aug 29	Sep 15
2017	KPC_L	June 1	85 (39)	June 15	Aug 25	Sep 12
	KPC_U	June 10	73 (16)	June 15	Aug 22	Sep 1
2018	KPC_L	June 20	66 (38)	July 1	Aug 25	Sep 20**
	KPC_U	June 26	51 (8)	July 12	Aug 16	Sep 19
2019	KPC_L	June 6	115 (61)	June 13	Sept 29	Sep 13
	KPC_U	June 12	67 (14)	June 13	Aug 18	Sep 11

https://doi.org/10.5194/tc-2021-45
Preprint. Discussion started: 2 March 2021

The Cryosphere Discussions

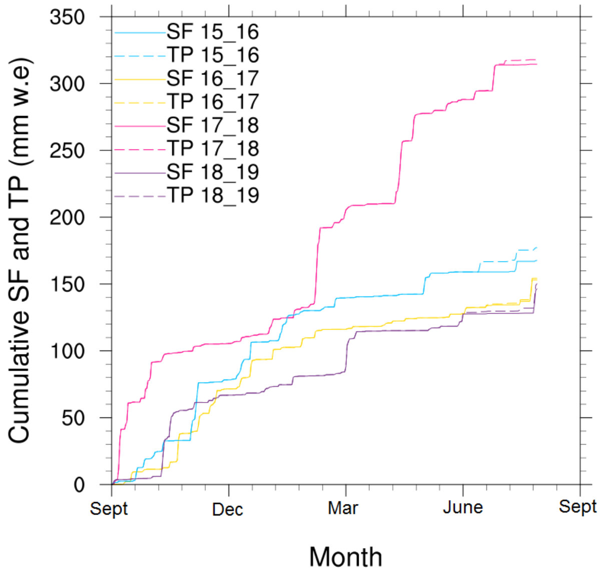

Figure 8: The cumulative total precipitation (TP) and snowfall (SF) from September (beginning of the accumulation season) to August (end of melt season) at KPC_L location from ERA5.

3.3.3 2018 Climate Conditions

The smallest total SGL area and latest lake development were observed in 2018. The latest observed onset of warm air temperatures was also in 2018, when the first recorded daily Ta above freezing was on June 20th (Figure 5; Table 2). The first two weeks of June were colder than in any other year in the last decade of observations (Figure 5). This is also reflected in the much colder June average Ta over the NEGIS region from the PWRF simulations (Figure 6c). All three summer months were characterised by considerably cooler air temperatures over the area of interest, with above freezing temperatures restricted to very low-lying parts of the glacier during July (Figure 7). June and July were both 2.0 °C cooler than average at both observation locations. Both the number of days above freezing and the consecutive number of days above freezing were both at their lowest in 2018 (Table 2), with just 8 consecutive days above freezing at KPC_U. In August, Ta picked up and were close to average conditions throughout August (Figure 5). The last day with Ta above freezing was observed on August 25 at KPC_L, the same as in 2017 (Table 2). However, the latest observation of SGLs at 370m a.s.l was September 18th, the latest in the four-year period, and SGLs were still visible at the end of the observational period (Table 2).

Despite the cooler conditions at both locations in summer 2018, positive biases in SWin were observed at both locations in July and August. The July SWin average was 32.7 Wm^{-2} and 18.4 Wm^{-2} higher than the 2009-2019 average at KPC_L and KPC_U, respectively. Similarly, the August SWin positive bias was 18.9 Wm^{-2} at KPC_L and 17.3 Wm^{-2} at KPC_U. Higher than average cloud cover in June (0.45 compared to 0.36 at KPC_U) and lower than average in July and August provide further evidence for clearer skies in the mid to late summer.

The largest amount of cumulated snowfall during the accumulation period (September to May) occurred in 2018 with 277.9 mm (Figure 8). In the other years of interest, the cumulated snowfall total was less than 190 mm. There were a number of large snowfall events in 2018 which contributed to the larger total precipitation. For example, between February 22 and February 26 2018, 56.5 mm w.e snowfall fell in the region, which is more than the winter

https://doi.org/10.5194/tc-2021-45
Preprint. Discussion started: 2 March 2021

(DJF) total snowfall in 2015/2016. The regular fresh snow episodes increased the albedo and reflected shortwave incoming radiation at the start of the summer season. A thick, fresh snowpack also has a low density, with more space for liquid water to penetrate instead of sitting on the surface in SGLs. The switch from SGL area increase (lake development) to decrease (freeze up) and back again during June 2018 (Figure 2) was due to a number of snowfall events in June, which covered any exposed SGLs. The continuous input of snowfall throughout the year and into summer delayed the onset of SGL development at 870m a.s.l to mid-July (Table 2), which was the latest in the four-year period,

In 2018, the spatial distribution of SGLs was different to the other three years, with the largest SGL area at elevations between 300m and 400m a.s.l (Figure 4). Very few SGLs were observed at elevations greater than 900m, leading to smaller average individual SGL area, as no larger lakes at higher elevations were identified (Figure 3). Average individual lake size in 2018 was 0.02 km^2, compared to 0.07 km^2 in 2016, 0.06 km^2 in 2017 and 2019.

A combination of the cooler air temperatures at the start of summer and thick snowpack led to the delayed onset of SGL development, lower maximum altitude of SGLs and lower total SGL area (Figure 3). The positive SWin and average temperatures towards the end of summer, together with a considerable amount of liquid water from the melted snowpack, likely provided optimal conditions for the later peak in maximum SGL area and slower freeze over of the lakes, with many still remaining open at the end of the observational period in September 2018 (Table 2).

3.3.4 2019 Climate Conditions

Summer 2019 received much media attention due to the long, early-season heat wave that stretched across most of continental Europe and Greenland. At lower elevations, the conditions in summer 2019 were remarkable. At both KPC_L and KPC_U, air temperature records were broken in June 2019 (Figure 5a,b), along with most areas of the ice sheet (Tedesco and Fettweis, 2020). There were 115 days of Ta greater than 0 °C with 61 of those being consecutively observed at KPC_L (Table 2). Similarly, warm Ta continued past the summer season, with the final observation of Ta above 0 °C on September 28th (Table 2). On June 12th, 2019, a new daily air temperature record was set at KPC_U of 4.2°C, swiftly broken by a new daily record on June 13th of 4.3°C. Prior to these two days, the highest temperature had been during the record-breaking summer of July 2012. Similarly, an hourly maximum of 7.9°C was recorded at KPC_U, which is the highest hourly temperature observation in a decade. Despite a warm start to the season, air temperatures returned to normal for the remainder of June and July. A second peak temperature event was recorded in early August 2019. The highest daily air temperature record at KPC_L (between 2009 and 2019) of 6.9°C was observed on August 2nd, 2019.

Some of the largest anomalies of SWin were observed in summer 2019, with KPC_L and KPC_U observing monthly negative anomalies of -30.0 Wm-2 and -19 Wm-2 respectively, for June, despite the high temperatures. Conversely, July saw opposite anomalies, with large positive anomalies in SWin at both KPC_L (+35.4 Wm-2) and KPC_U (+34.3 Wm-2). Similarly, the July average cloud cover was considerably below average, with a value of 0.24 compared to an average of 0.36 at KPC_U. A persistent high-pressure system was responsible for the early-season temperature and melt increases seen over the whole ice sheet (Tedesco and Fettweis, 2020). However, increased cloudiness observed in the northeast of the ice sheet (and also simulated by Tedesco and Fettweis, 2020) also contributed to the early melt onset in June.

The smallest accumulated snowfall from 2016 to 2019 occurred in 2019, with only 125 mm falling by May (Figure 7). The particularly shallow snowpack provides less water storage availability and lower albedo values, which likely led to the earlier SGL detection in 2019 compared to the other warmer than average year of 2016. The later refreeze of SGLs in the previous summer may also have contributed to the earlier detection in 2019. At the end of

https://doi.org/10.5194/tc-2021-45
Preprint. Discussion started: 2 March 2021

August, 21 mm of snowfall occurred, which started the new accumulation season earlier than in previous years (Figure 8). Between August 30th and September 16th there are very few melt ponds detected due to thick cloud cover (not shown). On September 20th, there is evidence of fresh snowfall and very few pond outlines remaining, providing further evidence for snowfall towards the end of August and start of September.

SGL development started earlier in 2019 than in 2016 despite both years observing Ta above 0°C at a similar time (June 6 in 2019 and June 7 in 2016) (Table 2). Total SGL area was largest in 2019, even though the average size of individual SGLs was the same as in 2017 (0.06 km^2). A combination of higher air temperatures, more days above freezing and a smaller snowpack at the start of the melt season all contributed to a significantly higher total SGL area in 2019 (Figure 4). The peak melt pond area at the start of August 2019 coincides with an air temperature peak of 6.9°C on August 2nd at KPC_L, the warmest daily Ta ever recorded here (Figure 5). As PWRF simulations were only available until 2018, we cannot provide an overview of the spatial distribution of the warm temperatures. However, satellite images reveal extensive surface melt pond formation, very thin and broken sea ice, and a 50 km^2 calving event of Spalte Glacier was also recorded this year (Figure 1b).

To summarise the climatic conditions: we find that a combination of above average air temperatures, a thin pre-summer snowpack and summer precipitation falling as rain during summer 2016 and 2019 led to the exposure of a large number of SGL over a much larger area than observed in the two other years. Conversely, a large amount of snowfall preceding the melt season and below average air temperatures in 2018 led to the development of very few SGLs, which were restricted to the lower elevation areas.

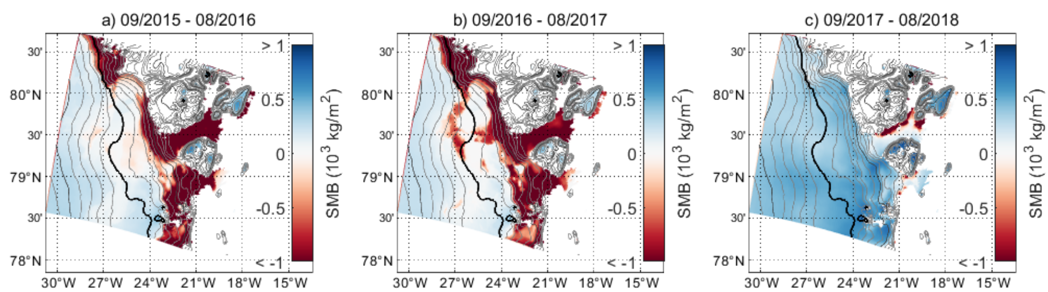

Figure 9: The annual surface mass balance of the 79°N glacier and NEGIS region from September to the following August in 2015-2016 (a), 2016-2017 (b), 2017-2018 (c). There are no estimates for 2018-2019 as the PWRF simulation which is used as input to the COSIPY SMB model was only available until December 2018. The dark black contour marks 1000m a.s.l and the grey contours are every 100m.

3.4 Surface mass balance

To assess whether high areas of SGL development relate to the Surface Mass Balance (SMB), the COSIPY SMB estimates from Blau et al. (in review) are used. COSIPY has been previously tested for a number of glaciers in Tibet (Sauter et al. 2020) and evaluated for 79°N Glacier by Blau et al. (in review). The SMB estimates from September to the following August for 2015 to 2018 are shown in Figure 9 (2018 to 2019 was not simulated, as COSIPY uses the PWRF output as atmospheric input). Spatially, the SMB is similar in 2015/2016 to 2016/2017, despite the warmer summer of 2016. Low-lying areas of the 79°N Glacier tongue, Zachariae Glacier and areas up to 1000 m a.s.l. were in a negative SMB area in 2015/2016. The following year, the negative SMB extends further inland and to higher altitudes up to 1300m a.s.l. The similarity in SMB between 2015/2016 and 2016/2017 is further presented in Figure 10.

Vertically, the annual SMB profiles are similar in 2015/2016 and 2016/2017 below 1000 m a.s.l. Only between 1000m and 1200m a.s.l. do the two years show differing conditions, although only by 0.2 kg m^{-1} (Figure 10a). The summer SMB remains negative up to elevations of 1400 m a.s.l. for both 2016 and 2017, which coincides with the approximate maximum elevations of SGLs in these years (Figure 4a, b). The annual and summer SMB in 2018 is considerably different to the previous two years. The annual SMB is negative only at elevations less than 100 m (Figure 10), which is restricted to areas of the floating tongue only (Figure 9). The summer SMB is also only negative up to 900m a.s.l. which also pinpoints the maximum elevation of SGLs in 2018 (Figure 4c).

It is likely that expansion of melt ponds at higher elevations is partly controlled by spikes in the SMB immediately prior to pond development, especially towards the end of the melt season. In summer 2017, SGL development at higher elevations occurred later in the melt season (Figure 3; yellow outlines at elevations greater than 900 m a.s.l. are only visible in August), despite the daily Ta already falling below 0°C. The week prior to July 20th, 2017 (Figure 3a), SMB was mostly positive at elevations greater than 900 m (Figure S2a), however for the five days prior to August 23rd, 2017 (Figure 3b), SMB returned to negative at these higher altitudes (Figure S2b), despite an overall trend towards a positive SMB at lower elevations (Figure S2c). Therefore, not only the local meteorology controls the SGL development, especially at higher elevations.

4 Discussion

Summer 2016 saw the largest loss of glacier area since 2012, which was the standout, record-breaking melt year since records began (Hanna et al. 2014a). More recently, summer 2019 again broke records for melting and temperatures. Similar to previous studies in the Antarctic (Kingslake et al 2015, Langley et al. 2016), we find a strong relationship between air temperature and lake development. Previously, Langley et al. (2016) hypothesized that lake expansion in the early part of the season is particularly rapid, as even small changes in air temperature can increase the total lake area. A rapid increase in lake area was seen at the start of the 2016 and 2019 melt season over 79°N glacier, however in 2017, late-summer temperatures led to later expansion of SGLs. The very large rate of increase at the start of summer 2016 (Figure 2) is likely skewed by the slightly lower temporal resolution in 2016 (approximately 3-7 days) compared to the other years (1-2 day). In 2016 and 2017, there was a lower temporal coverage than the following years as only one Sentinel satellite was in orbit and data quality was poorer (Hochreuther et al. 2021). However, upon visual inspection of the satellite images, 2016 also saw a rapid expansion in SGLs, similar to 2019.

https://doi.org/10.5194/tc-2021-45
Preprint. Discussion started: 2 March 2021

The Cryosphere
Discussions

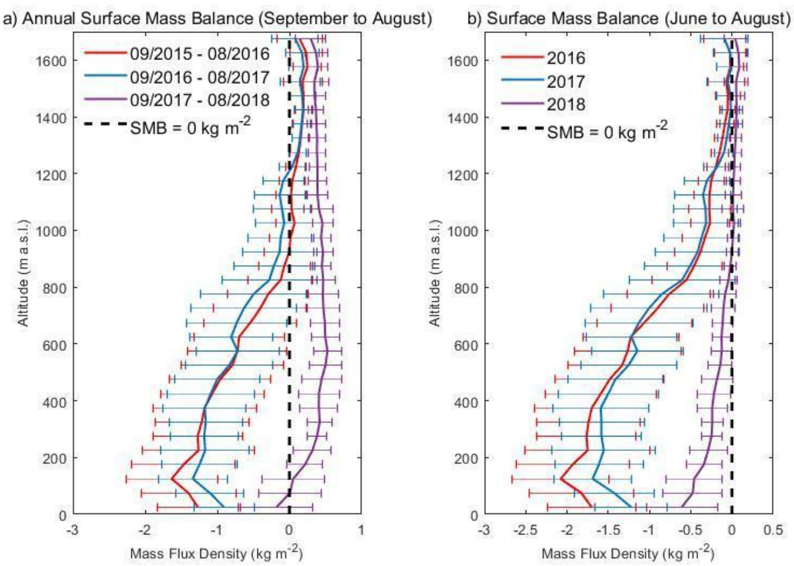

Figure 10: The annual (a) and summer (JJA) surface mass balance between September 2015 and August 2018, averaged over each altitude in 50m bands. Error bars indicate the standard deviation of SMB for each grid in the respective altitude band.

For the Shackleton glacier in Antarctica, the years with largest SGL area and volume were not always in the same years as the highest summer near-surface air temperatures (Arthur et al. 2020). With only four years of data in the present study, no major conclusions can be drawn on this, however it is clear that precipitation also had an impact on SGL area and development over northeast Greenland. In Buzzard (2018b), the relationship between snowfall and melt pond depth was not simple or linear. A small amount of snowfall will promote melt pond development, as there is more water available at the surface, however too much accumulation can bury the melt pond (especially if the surface has started to freeze towards the end of summer) and reduce melting (Buzzard et al 2018b). We also see evidence of this non-linear response. A combination of a large amount of snowfall prior to the 2018 melt season, and below average summer air temperatures led to a lower total area of SGLs and positive mass balance over the majority of the glacierized area (Figure 9, 10). With a thicker snowpack, it took longer for the SGLs to form, as there was more pore space for water to percolate through before pooling. A similar conclusion was found for Tibeten glaciers (Mölg et al. 2012) and Shackleton ice shelf in the Antarctic (Arthur et al. 2020). Arthur et al. (2020) found that higher accumulation rates contribute to higher firn air content, which allows more water to be retained within the snowpack rather than pooling into SGLs. The higher snowfall in 2018 also created the conditions which allowed the lakes to remain open for longer than in previous years, because more water was available towards the end of the melt season.

Conversely, the year with the smallest snowfall amount (2018-2019 accumulation season) was not followed by the summer with the fewest melt ponds. However, the much higher air temperatures and late summer freeze up of SGLs in 2018 played a bigger role. Summer 2016 saw the second largest SGL area and spatial spread. This year also saw a large amount of precipitation fall as rainfall in summer. Rainfall is additional liquid for the surface of the glacier, provides heat to the snowpack and refreezes into solid ice lenses which preconditions the glacier surface for further SGL development (Machguth et al. 2016). Rainfall associated with summer storms has been linked to extreme melting events in southern Greenland by Oltmanns et al. (2019) and enhanced ice velocity in western Greenland by Doyle et al.

https://doi.org/10.5194/tc-2021-45
Preprint. Discussion started: 2 March 2021

(2015). Similarly, Tedesco and Fettweis (2020) concluded that low snow accumulation was also partly responsible for the extensive melting along much of the coast of Greenland in 2019

The dominant mode of variability for Greenland and the Arctic is the North Atlantic Oscillation (NAO), defined as the ‘seesaw’ of atmospheric surface pressure changes between Iceland and the Azores (Hildebrandsson 1897, Hanna et al 2014b). Three other modes of variability were found to be important for specifically the northeast and east of Greenland by Lim et al (2016): the Arctic Oscillation (AO), the East Atlantic (EA) pattern, and the Greenland Blocking Index (GBI). Generally (for the whole of Greenland), a negative phase of the NAO and AO are associated with a warm and dry atmosphere over the GIS, and often leads to mass loss at the surface (Lim et al 2016). Similarly, a strong negative NAO (< -0.5) combined with a strongly positive EA (> +0. 5) has led to significantly larger warming over the GIS in the most recent years, when compared to a negative or weakly positive EA combination (Lim et al 2016). Furthermore, a positive GBI (especially when combined with a positive EA and negative NAO) also leads to positive temperature anomalies over the GIS.

In 2016 and 2019, the average JJA NAO index was strongly negative (-1.36 for 2016, -1.23 for 2019) (see Supplementary material for teleconnection data). Simultaneously, both the JJA EA index and the GBI were strongly positive in both of these years. (1.44 and 1.73 respectively). In summer 2016, the EA (GBI) JJA average was 1.44 (1.73). Similarly, in 2019 the JJA average EA index (GBI index) was 1.1 (2.26). This combination of strong -NAO and strong +EA also occurred in both summer 2010 and 2012, when extensive melting was observed over the GIS (Lim et al 2016). In terms of teleconnections, the biggest differences between 2016/2019 and the 2017/2018 summers was the NAO and GBI summer indices. In 2017 the NAO index was positive in June and July. In 2018 the JJA NAO index was strongly positive (1.74), with all summer months observing a +NAO signal. The GBI for summer 2017 and 2018 was weakly negative (-0.03) and negative (-0.57) respectively. In terms of the teleconnection indices evaluated here, summer 2017 appears to the be the intermediate or transition year between a particularly strong negative NAO in 2016 and a strong positive NAO in 2018. A decreasing trend in summer NAO since 1981 has been previously identified and is believed to be partly responsible for record-breaking warm temperatures over Greenland in the most recent decade (Hanna et al. 2014).

The relationship between teleconnections and precipitation is more complicated and is often only significant in the southern part of Greenland where the majority of the precipitation falls. Bjork et al (2018) identified a positive relationship between NAO and precipitation in eastern Greenland: there is more precipitation during +NAO years. The year with the largest cumulative precipitation amounts was the 2017-2018 accumulation season, which was also characterised by a strong +NAO index. However, the relationship between NAO and precipitation for NE Greenland cannot be assessed with certainty in this study.

Although we present only four years of results here and previous studies in this region are sparse, we are confident that SGLs are a persistent feature in the NEGIS and 79°N region. Sundal et al. (2009) observed SGLs between 2003 and 2007 using MODIS data. With the availability of very-high resolution (10 m) Sentinel data, the SGL areas are less erroneous than previously stated using lower-resolution MODIS data (250 m) (Hochreuther et al. 2021). There is an increase in the maximum altitude of SGL detection between the early 2000’s study of Sundal et al (2009) (1200m a.s.l) and the results presented here (1400m a.s.l). The lakes at these higher elevations are larger and therefore would have been detected by the MODIS data in the Sundal et al. (2009) study, were they present. Therefore, it is likely that maximum lake altitude has increased over time.

This is not surprising given an increasing air temperature trend of 0.8°C decade^{-1} over 79°N Glacier (Turton et al. 2019), and model suggestions of inland expansion in this area into the 21st century (Ignéczi et al. 2016). Leeson et al. (2015) concluded that maximum lake altitude could reach up to 2221m a.s.l with RCP 8.5 future projections. Although there are a number of assumptions made in our comparison to Sundal et al. (2009), it is possible that inland expansion of lakes is occurring under increased air temperatures in this region.

Under certain high-melt years, surface rivers have been observed for a number of northern Greenland glaciers, including 79°N (Bell et al. 2017). Whilst in the current study, we remove the melt water channels to focus on SGLs only, a number of linear features similar to rivers are clearly visible in the Sentinel data (Figure S1). This highlights that more liquid water is likely present on and within the glacier than discussed here. There is even some evidence of the persistence of liquid water in melt lakes during the winter season in this region. Schröder et al. (2020) used Sentinel 1 SAR data which can detect water without the presence of sunlight (unlike optical sensors such as Sentinel 2) and under the snow surface. It is hypothesised that lakes beneath the surface were formed in particularly warm years (such as 2019) and then subsequently covered by a thin ice lens or snow (Schröder et al. 2020).

5 Conclusions

In this study we provide a multi-year analysis of the area of SGLs over the North East Greenland Ice Stream and investigate the atmospheric and topographic controls of the evolution of the lakes. SGLs have been automatically detected using the Hochreuther et al (2021) method, from 2016 to 2019. Whilst the SGL location is primarily determined by topographic depressions and the slope of the ice sheet, the occurrence of lakes within these depressions relies on the local meteorology and SMB.

Similar to the location of lakes, the maximum size of individual lakes is controlled by topography. At higher elevations, larger lakes form due to a lower slope angle (Figure 4).

The higher SGL areas in 2016 and 2019 were due to more lakes developing at higher elevations on the ice sheet, as opposed to individual lakes becoming larger. SGLs refreeze and melt in the same locations above the grounding line each year, but maximum inland expansion of the lakes depends on climatic conditions. Schröder et al. (2020) state that liquid water remains in the lakes throughout the year but can become buried by an ice lens or snow which prohibits the detection by optical sensors. It is therefore possible that in warmer years, such as 2019, the snowpack and lens are melted to reveal melt lakes formed previously, which contributes to the larger lake area.

The melt detection algorithm implemented here and developed by Hochreuther et al. (2021) is automated, meaning that this work can be continued in the future to analyse a long-term time series of SGL evolution. Our findings would ideally now be expanded to include volume estimates and to model the surface and subglacial hydrology to provide an estimate of the volume of fresh water entering the ocean. Estimates of the volume are not provided in this study, which is unusual for these types of studies (e.g Pope et al. 2016., Arthur et al. 2020). We hypothesise that SGLs in this region are much deeper than those observed in the west of Greenland. Neckel et al. (2020) recorded the depth of an SGL on the 79°N Glacier, which, at the edge of the lake, had a depth of 10.8 m. The same lake drained suddenly in September 2017, and analysis of the height difference from a full to empty lake using DEMs revealed a subsidence of 50 m in the centre of the lake (Neckel et al. 2020). Therefore, applying the same albedo-depth calculation to the lakes in northeast Greenland as in western Greenland would largely underestimate the volumes. In-situ observations of these lakes are required to calculate depth and volume with a different albedo-depth coefficient.

Below average air temperatures and high snowfall accumulation prior to the melt season of 2018 contributed to reduced lake extent, a reduced amplitude in the seasonal cycle of lake evolution and late season freeze up of the SGLs. These climatic conditions led to a largely positive mass balance at all altitudes except the very lowest lying regions. Conversely, in the prior two years, surface mass balance was negative for a large portion of 79°N and the surrounding area. Largely this was driven by the above average air temperature, evident in both the in-situ AWS data (Figure 5) and in the regional atmospheric modelling output (Figure 6, 7).

Whilst 2019 was record breaking in terms of melt over much of the Greenland ice sheet, in fact second only to 2012 (Tedesco and Fettweis, 2020), the summer of 2016 was only warm and extreme in the northeast region, highlighting the importance of regional studies of extreme melting, as well as the Greenland ice sheet-wide studies.

6 Data Availability

The daily average surface mass balance data is available at: https://doi.org/10.5281/zenodo.4434259. For higher temporal resolution see Blau et al. (in review). The daily average PWRF data is available at: https://doi.org/10.17605/OSF.IO/53E6Z. For higher temporal resolutions see Turton et al. (2020). Lake outline polygons and cloud masks are available on request and are currently being uploaded to Pangaea Data Centre, pending a DOI.

7 Author Contribution

J.V.T wrote the manuscript and conducted the climatological analysis. P.H developed and applied the automatic detection algorithm for the SGLs and assisted in discussing the results. N.R assisted in the development of the algorithm and writing the manuscript. M.T.B. conducted the SMB modelling and analysis.

8 Competing Interests

The authors declare no conflict of interest.

9 Acknowledgements

We are grateful to the European Space Agency (ESA) for providing the Sentinel-2 data and to the Greenland and Denmark Geological Survey (GEUS) for maintaining the AWS and providing the data. We acknowledge the German Federal Ministry for Education and Research (BMBF) for funding this work as part of the GROCE project (Greenland Ice Sheet/Ocean Interaction) (Grant 03F0778F. We also thank the High-Performance Computing Centre (HPC) at the University of Erlangen-Nürnberg's Regional Computation Centre (RRZE) for their support and resources.

10 References

Arthur, J.F., Stokes, C.R., Jamieson, S.S.R., Carr, J.R. and Leeson, A.A.: Distribution and seasonal evolution of supraglacial lakes on Shackleton Ice Shelf, East Antarctica. The Cryosphere, 14 (11), 4103-4120, doi:10.5194/tc-14-4103-2020, 2020.

Blau, M.T., Turton, J.V., Mölg, T. and Sauter, T.: Surface mass and energy balance estimates of the 79N Glacier (Northeast Greenland) linking COSIPY and Polar WRF. J. Glaciology. In review.

Bell, R.E., Chu, W., Kingslake, J., Das, I., Tedesco, M., Tinto, K.J., Zappa, C.J., Frezzotti, M., Boghosian, A., Sang Lee, W.: Antarctic ice shelf potentially stabilized by export of meltwater in surface river, Nature, 544, 344-348, doi:10.1038/nature22048, 2017.

Bonne, J-L., Steen-Larsen, H.C., Risi, C., Werner, M., Sodemann, H., Lacour, J-L., Fettweis, X., Cesana, G., Delmotte, M., Cattani, O., Vallelonga, P., Kjae, H.A., Clerbaux, C., Sveinbjörnsdottir, A.E. and Masson-Delmotte, V.: The summer 2012 Greenland heat wave: in situ and remote sensing observations of water vapor isotopic composition during an atmospheric river event. JGR: Atmospheres, 120, (7), 2970-2989, doi:10.1002/2014JD022602, 2015.

Buzzard, S.C., Feltham, D.L. and Flocco, D.: A mathematical model of melt lake development on an ice shelf. J. Advances in Modeling Earth Systems, 10 (2), 262-283, doi:10.1002/2017MS001155, 2018a

https://doi.org/10.5194/tc-2021-45
Preprint. Discussion started: 2 March 2021

Buzzard, S.C., Feltham, D. and Flocco, D.: Modelling the fate of surface melt on the Larsen C ice shelf. The Cryosphere, 12 (11), 3565-3575, doi:10.5194/tc-12-3565-2018, 2018b.

Das, S.B., Joughin, I., Behn, M.D., Howat, I.M., King, M.A., Lizarralde, D. and Bhatia, M.P.: Fracture propagation to the base of the Greenland Ice Sheet during supraglacial lake drainage. Science, 320 (5877), 778-781, doi:10.1126/science.1153360, 2008.

Doyle, S.H., Hubbard, A., van de Wal, R.S.W., Box, J.E… Hubbard, B.: Amplified melt and flow of the Greenland ice sheet driven by late-summer cyclonic rainfall. Nat Geosci. 8, 647-653, doi:10.1038/ngeo2482, 2015

Flowers, G.: Hydrology and the future of the Greenland Ice Sheet. Nature Comms. 9, 2729, doi:10.1038/s41467-018-05002-0, 2018.

Hanna, E., Fettweis, X., Mernild, S.H., Cappelen, J., Ribergaard, M.H., Shuman, C.A., Steffen, K.,Wood, L. and Mote, R.L.: Atmospheric and oceanic climate forcing of the exceptional Greenland ice sheet surface melt in summer 2012. Int. J. Climatology, 34, 1022-1037, doi:10.1002/joc.3743, 2014a

Hanna, E., Cropper, T.E., Jones, P.D., Scaife, A.A. and Allan, R.: Recent seasonal asymmetric changes in the NAO (a marked summer decline and increased winter variability) and associated changes in the AO and Greenland Blocking Index. Int. J. climatology, 35 (9), 2540- 2554, doi:10.1002/joc.4157, 2014b

Hildebrandsson, H.H.: Quelques recherches sur les centres d'action de l'atmosphere, I-IV. Kungliga Svenska Vetenskaps-Akademiens Handlingar, 29 (3), 36. 1897.

Hines, K. M., Bromwich, D. H., Bai, L., Bitz, C. M., Powers, J. G., Manning, K. W.: Sea Ice Enhancements to Polar WRF*. Mon. Weather Rev., 143(6), 2363-2385, doi:10.1175/MWR-D-14-00344.1, 2015.

Hochreuther, P., Neckel, N., Reimann, N., Humbert, A. and Braun, M.: Fully automated detection of supra-glacial lake area for northeast Greenland using Sentinel-2 time series. Remote sensing, 13(2), 205, doi:10.3390/rs13020205, 2021.

Igneczi, A., Sole, A.J., Livingstone, S.J., Leeson, A.A., Fettweis, X., Selmes, N., Gourmelen, N. and Briggs, K.: Northeast sector of the Greenland ice sheet to undergo the greatest expansion of supraglacial lakes during the 21st century. Geophysical research letters. 43 (18), 9729-9738, doi:10.1002/2016GL070338, 2016.

Khan, S. A., Kjær, K. H., Bevis, M., Bamber, J. L., Wahr, J., Kjeldsen, K. K., Bjørk, A.A., Korsgaard, N.J., Stearns, L.A., van den Broeke, M.R, Liu, L., Larsen, N.K. and Muresan, I. S: Sustained mass loss of the northeast Greenland ice sheet triggered by regional warming. Nature Climate Change, 4(4), 292–299, doi:10.1038/nclimate2161, 2014.

Kingslake, J., Ng, F. and Sole, A.: Modelling channelized surface drainage of supraglacial lakes. J. Glaciology, 61, doi:10.3189/2015JoG14J158, 2015

Krieger, L., Floricioiu, D. and Neckel, N.: Drainage basin delineation for outlet glaciers of northeast Greenland based on Sentinel-1 ice velocities and TanDEM-X elevations. Remote sensing of the environment, 237, 111483, doi:10.1016/j.rse.2019.111483, 2020.

Lampkin, D.J. and VanderBerg, J.: A preliminary investigation of the influence of basal and surface topography on supraglacial lake distribution near Jakobshavn Isbrae, western Greenland. Hydrological Processes, 25, 3347-3355, doi:10.1002/hyp.8170, 2011.

Langley, E.S., Leeson, A.A., Stokes, C.R., Jamieson, S.S.R.: Seasonal evolution of supraglacial lakes on an East Antarctic outlet glacier, Geophys. Res. Lett., 43, doi:10.1002/2016GL069511, 2016.

Leeson, A.A., Shepherd, A., Briggs, K., Howat, I., Fettweis, X., Morlighem, M. and Rignot, E.: Supraglacial lakes on the Greenland ice sheet advance inland under warming climate. Nature Climate Change. 5, 51-55, doi:10.1038/nclimate2463, 2015.

Leeson, A.A., Forster, E., Rice, A., Gourmelen, N., van Wessem, J.M.: Evolution of supraglacial lakes on the Larsen B ice shelf in the decades before it collapsed, Geophys. Res. Lett., 47, doi:10.1029/2019GL085591, 2020.

https://doi.org/10.5194/tc-2021-45
Preprint. Discussion started: 2 March 2021

Lim, Y-K., Schubert, S.D., Nowicki, S.M.J., Lee, J.N., Molod, A.M., Cullather, R.I., Zhao, B. and Velicogna, I.: Atmospheric summer teleconnections and Greenland Ice Sheet surface mass variations: insights from MERRA-2. Environmental Research Letters, 11 (2), 024002, doi:10.1088/1748-9326/11/2/024002, 2016.

Luckman, A., Elvidge, A., Jansen, D., Kulessa, B., Kuipers Munneke, P., King, J. and Barrand, N.E.: Surface melt and ponding on Larsen C ice shelf and the impact of foehn winds. Antarctic Science, 26 (6), 625-635, doi:10.1017/S0954102014000339, 2014.

Lüthje, M., Pedersen, L.T., Reeh, N. and Greuell, W.: Modelling the evolution of supraglacial lakes on the West Greenland ice-sheet margin. J. Glaciology, 52 (179), 608-618, doi:10.3189/172756506781828386, 2006.

MacFerrin, M., Machguth, H., van As, D… Abdalati, W.: Rapid expansion of Greenland's low permeability ice slabs. Nature, 573, 403-407. Doi:10.1038/s41586-019-1550-3, 2019.

Machguth, H., MacFerrin, M., van As, D., Box, J.E., Charalampos, C., Colgan, W., Fausto, R.S., Meijer, H, Mosley-Thomposon, E. and van de Wal, R.S.W.: Greenland meltwater storage in firn limited by near-surface ice formation. Nat. Clim. Change, 6, 390-393, doi:10.1038/nclimate2899, 2016.

Malinka, A., Zege, E., Istomina, L., Heygster, G., Spreen, G., Perovich, D. and Polashenski, C.: Reflective properties of melt ponds on sea ice. The Cryosphere, 12 (6), 1921-1937, doi:10.5194/tc-12-1921-2018, 2018.

Mayer, C., Schaffer, J., Hattermann, T., Floricioiu, D., Krieger, L., Dodd, P. A., … Schannwell, C: Large ice loss variability at Nioghalvfjerdsfjorden Glacier, Northeast Greenland, Nature Comms, 9(1), 2768, doi:10.1038/s41467-018-05180-x, 2018.

Mölg, T., Maussion, F., Yang, W. and Scherer, D: The footprint of Asian monsoon dynamics in the mass and energy balance of a Tibetan glacier, The Cryosphere, 6, 1445-1462, doi:10.5194/tc-6-1445-2012, 2012.

Mouginot, J., Rignot, E., Scheuchl, B., Fenty, I., Khazendar, A., Morlighem, M., Buzzi, A. and Paden, J.: Fast retreat of Zachariae Isstrøm, northeast Greenland. Science, 350 (6266), 1357-1361, doi:10.1126/science.aac7111, 2015.

Neckel, N., Zeising, O., Steinhage, D., Helm, V. and Humbert, A.: Seasonal observations at 79°N Glacier (Greenland) from remote sensing and in situ measurements. Frontiers Earth Sci., 8 (142), doi:10.103389/feart.2020.00142, 2020.

Noël, B., van de Berg, W.J., Lhermitte, S. and van den Broeke, M.: Rapid ablation zone expansion amplifies north Greenland mass loss. Science Advances, 5 (9), eaaw0123, doi:10.1126/sciadv.aaw0123, 2019.

Oltmanns, M., Straneo, and Tedesco, M.: Increased Greenland melt triggered by large scale, year-round cyclonic moisture intrusions. The Cryosphere, 13 (3), 815-825, doi:10.5194/tc-13-815-2019, 2019.

Perovich, D.K., Grenfell, T.C., Light, B. and Hobbs, P.V.: Seasonal evolution of the albedo of multiyear Arctic sea ice, JGR: Oceans, 107 (C10), 20-1 – 20-13, doi:10.1029/2000JC000438, 2002.

Polar Weather Research and Forecasting Model, developed by Ohio State University, available from: http://polarmet.osu.edu/PWRF/, last accessed: July 29 2019.

Pope, A., Scambos, T.A., Moussavi, M., Tedesco, M., Willis, M., Shean, D. and Grigsby, S.: Estimating supraglacial lake depth in West Greenland using Landsat 8 and comparison with other multispectral methods, The Cryosphere, 10 (1), 15-27, doi:10.5194/tc-10-15-2016, 2016

Rathmann, N.M., Hvidberg, C.S., Solgaard, A.M., Grinsted, A., Gudmundsson, H., Langen, P.L., Nielsen, K.P. and Kusk, A.: Highly temporally resolved response to seasonal surface melt of the Zachariae and 79N outlet glaciers in northeast Greenland. Geophysical Research Letters, 44 (19), 9805-9814, doi:10.1002/2017GL074368, 2017.

Sauter, T., Arndt, A. and Schneider, C.: COSIPY v1.3 – an open-source coupled snowpack and icesurface energy and mass balance model. Geosci. Model Dev. 13, 5645-5662,doi:10.5194/gmd-13-5645-2020, 2020

https://doi.org/10.5194/tc-2021-45
Preprint. Discussion started: 2 March 2021

Schröder, L., Neckel, N., Zindler, R. and Humbert, A.: Perennial Supraglacial Lakes in Northeast Greenland Observed by Polarimetric SAR. Remote sensing, 12, 2798, doi:10.3390/rs12172798, 2020.

Smith, L., Yang, K., Pitcher, L.H., Overstreet, B.T., Chu, V.W., Rennermalm, A.K., Ryan, J.C., …Behar, A.E: Direct measurements of meltwater runoff on the Greenland ice sheet surface, PNAS, 114 (50), E10622-E10631, doi10.1073/pnas.1707743114, 2015.

Sundal, A.V., Shepherd, A., Nienow, P., Hanna, E., Palmer, S. and Huybrechts, P.: Evolution of supra-glacial lakes across the Greenland Ice Sheet. Remote sensing of Environment, 113, 2164-2171, doi:10.1016/j.rse.2009.05.018, 2009.

Tedesco, M., Lüthke, M., Steffen, K., Steiner, N., Fettweis, X., Willis, I., Bayou, N. and Banwell, A.: Measurement and modeling of ablation of the bottom of supraglacial lakes in western Greenland. Geophysical Research Letters, 39, L02502, doi:10.1029/2011GL049882, 2012.

Tedesco, M., Fettweis, X., Mote, T., Wahr, J., Alexander, P., Box, J. E., and Wouters, B: Evidence and analysis of 2012 Greenland records from spaceborne observations, a regional climate model and reanalysis data, The Cryosphere, 7(2), 615–630, doi:10.5194/tc-7-615-2013, 2013.

Tedesco, M. and Fettweis, X.: Unprecedented atmospheric conditions (1948-2019) drive the 2019 exceptional melting season over the Greenland ice sheet. The Cryosphere, 14 (4), 1209-1223, doi:10.5194/tc-14-1209-2020, 2020.

Turton, J. V., Mölg, T. & Van As, D: Atmospheric Processes and Climatological Characteristics of the 79N Glacier (Northeast Greenland), Mon. Weather Rev., 147(4), 1375–1394, doi:10.1175/MWR-D-18-0366.1, 2019a.

Turton, J. V., Mölg, T and Collier, E: NEGIS_WRF model output, Open Science Framework Repository, last accessed October 1 2019, doi: /10.17605/OSF.IO/53E6Z, 2019b.

Turton, J.V., Mölg, T and Collier, E: High-resolution (1 km) Polar WRF output for 79°N Glacier and the northeast of Greenland from 2014 to 2018, Earth System Science Data, 12, 1191-1202, doi:10.5194/essd-12-1191-2020, 2020.

van As, D., and Fausto, R: Programme for Monitoring of the Greenland Ice Sheet (PROMICE): first temperature and ablation records. Geolog. Survey Denmark Greenland Bulletin, 23, 73–76, doi:10.34194/geusb.v23.4876, 2011.

Vijay, S., Khan, S.A., Kusk, A., Solgaard, A.M., Moon, T. and Bjørk, A.A.: Resolving seasonal ice velocity of 45 Greenlandic glaciers with very high temporal details. Geophysical Research Letters, 46 (3), 1485-1495, doi:10.1029/2018GL081503, 2019.

Wang, C., Graham, R.M., Wang, K., Gerland, S. and Granskog, M.A.: Comparison of ERA5 and ERA-Interim near surface air temperature, snowfall and precipitation over Arctic sea ice: effects on sea ice thermodynamics and evolution. The Cryosphere, 13, 1661-1679, doi:10.5194/tc-13-1661-2019, 2019

Yang, K., Smith, L.C., Fettweis, X., Gleason, C.J., Lu, Y. and Li, M: Surface meltwater runoff on the Greenland ice sheet estimated from remotely sensed supraglacial lake infilling rate. Remote Sensing of Environment, 234, 111459, doi:10.1016/j.rse.2019.111459, 2019.

Zwally, H.J., Abdalati, W., Herring, T., Larson, K., Saba, J. and Steffen, K.: Surface melt-induced acceleration of Greenland ice sheet flow. Science, 297 (5579), 218-222, doi:10.1126/science.1072708, 2002.